

## REVERBERATION MAPPING WITH INTERMEDIATE-BAND PHOTOMETRY: DETECTION OF BROAD-LINE H $\alpha$ TIME LAGS FOR QUASARS AT $0.2 < Z < 0.4$

LINHUA JIANG<sup>1</sup>, YUE SHEN<sup>2,3</sup>, IAN D. MCGREER<sup>4</sup>, XIAOHUI FAN<sup>4</sup>, ERIC MORGANSON<sup>3,5</sup>, AND ROGIER A. WINDHORST<sup>6</sup>

*Draft version October 14, 2021*

### ABSTRACT

We present a reverberation mapping (RM) experiment that combines broad- and intermediate-band photometry; it is the first such attempt targeting a sample of 13 quasars at  $0.2 < z < 0.9$ . The quasars were selected to have strong H $\alpha$  or H $\beta$  emission lines that are located in one of three intermediate bands (with FWHM around 200 Å) centered at 8045, 8505, and 9171 Å. The imaging observations were carried out in the intermediate bands and the broad  $i$  and  $z$  bands using the prime-focus imager 90Prime on the 2.3m Bok telescope. Because of the large ( $\sim 1$  deg<sup>2</sup>) field-of-view (FoV) of 90Prime, we were able to include the 13 quasars within only five telescope pointings or fields. The five fields were repeatedly observed over 20–30 epochs that were unevenly distributed over a duration of 5–6 months. The combination of the broad- and intermediate-band photometry allows us to derive accurate light curves for both optical continuum (from the accretion disk) and line (from the broad-line region, or BLR) emission. We detect H $\alpha$  time lags between the continuum and line emission in 6 quasars. These quasars are at a relatively low redshift range  $0.2 < z < 0.4$ . The measured lags are consistent with the current BLR size-luminosity relation for H $\beta$  at  $z < 0.3$ . While this experiment appears successful in detecting lags of the bright H $\alpha$  line, further investigation is required to see if it can also be applied to the fainter H $\beta$  line for quasars at higher redshifts. Finally we demonstrate that by using a small telescope with a large FoV, intermediate-band photometric RM can be efficiently executed for a large sample of quasars at  $z > 0.2$ .

*Subject headings:* Galaxies: active — quasars: general — quasars: emission lines — quasars: supermassive black holes

### 1. INTRODUCTION

AGN reverberation mapping (RM; Blandford & McKee 1982; Peterson 1993) measures the light travel time (i.e., lags) between different regions of an AGN, most commonly the time lag between the UV/optical continuum (from the accretion disk) and the broad line (from the broad-line region, or BLR) emitting regions. RM is a powerful tool for probing the structure and kinematics of AGN BLRs. RM is used to estimate the masses of AGN central supermassive black holes (SMBHs), by combining the relation between the BLR size and AGN luminosity (the  $R$ – $L$  relation) with the assumption of virialized motions of clouds in the BLR. Through application of this method, RM has been established as the primary *direct* SMBH mass estimation technique for AGN/quasars at  $z \leq 0.1$ .

RM campaigns are expensive and time-consuming. They require repeated observations of individual targets with sufficient cadence over durations of a few months to a few years, depending on the source redshift and luminosity. The success rate also relies on other factors,

such as whether the variability of the target is significant or not during the RM campaign, which is usually unpredictable. To date RM experiments have been successful for about 60 AGN/quasars (e.g. Kaspi et al. 2000, 2005; Peterson et al. 2002, 2004, 2014; Bentz et al. 2009, 2013; Denney et al. 2009, 2010; Rafter et al. 2011, 2013; Barth et al. 2011, 2015; Du et al. 2014, 2015; Wang et al. 2014; Hu et al. 2015). A more detailed history of AGN RM experiments is summarized in a few recent works (e.g. Bentz et al. 2013; Bentz 2015; Peterson 2014; Shen et al. 2015a).

The majority of the above RM work was done with low-redshift AGN at  $z \leq 0.2$ . Much higher-redshift ( $z \geq 1$ ) AGN/quasars have also been tried (e.g. Metzroth et al. 2006; Kaspi et al. 2007; Trevese et al. 2007), yet the number of the successful detections of time lags is still very small. Recently the SDSS Reverberation Mapping program (SDSS-RM; Shen et al. 2015a) has enabled a new method of carrying out RM experiments. The SDSS-RM program is a dedicated multi-object RM campaign that simultaneously targeted 849 quasars in a single 7 deg<sup>2</sup> field. Based on the SDSS-RM data, Shen et al. (2015b) have reported their first detections of time lags in a sample of quasars at  $z \geq 0.3$ .

Traditional RM programs use spectroscopic observations to monitor the variability of continuum and line emission. Recently, photometric RM has been proposed or performed (e.g. Haas et al. 2011; Zu et al. 2013; Chelouche & Daniel 2012; Chelouche et al. 2014). The basic idea is to take photometry in two bandpasses, with one bandpass ‘on’ an emission line and the other one ‘off’ the line. The combination of the two measurements

<sup>1</sup> Kavli Institute for Astronomy and Astrophysics, Peking University, Beijing 100871, China; jiangKIAA@pku.edu.cn

<sup>2</sup> Department of Astronomy, University of Illinois at Urbana-Champaign, Urbana, IL 61801, USA

<sup>3</sup> National Center for Supercomputing Applications, University of Illinois at Urbana-Champaign, Urbana, IL 61801, USA

<sup>4</sup> Steward Observatory, University of Arizona, 933 North Cherry Avenue, Tucson, AZ 85721, USA

<sup>5</sup> Max-Planck-Institut für Astronomie, Königstuhl 17, 69117 Heidelberg, Germany

<sup>6</sup> School of Earth and Space Exploration, Arizona State University, Tempe, AZ 85287, USA

is used to derive the continuum and line fluxes. The advantage of the photometric RM is that it does not require spectroscopic observations, and can be easily performed with small telescopes. The challenge is the small contribution of the emission line flux to the total bandpass flux within a broad band, so that the photometric uncertainties significantly hamper measurements of variability in the line fluxes. Alternatively, one may use a narrow band with a full width at half maximum (FWHM) of a few tens Å (up to  $\sim 120$  Å) to cover the emission line. This has been done for a few local AGN at  $z < 0.05$  (e.g. Haas et al. 2011; Ramolla et al. 2013; Pozo Nuñez et al. 2015). In this case, the line flux contributes a large fraction of the total flux in the narrow band and line variability is more readily detected.

In this paper we present our intermediate-band reverberation mapping (IBRM) project, which uses the combination of broad and intermediate bands (with FWHM around 200 Å) to perform photometric RM. The usage of intermediate bands has the following two advantages, in addition to the general advantages of photometric RM mentioned above. An intermediate band can usually cover a whole emission line, while the line flux still contributes a significant fraction of the total flux in the band, if the line is selected to have high equivalent width (EW) as we do for the IBRM program. Secondly, it has a larger (compared to narrow bands) dynamic range in wavelength that allows the inclusion of more than one targets per field, which substantially increases observing efficiency. In our IBRM program, we observed 13 quasars within five fields or telescope pointings, and successfully detected time lags in 6 of them.

The structure of the paper is as follows. In Section 2 we present our quasar sample selection and their optical spectra. In Section 3 we introduce our IBRM campaign and the details of observations and data reduction. We derive the light curves and time lags of the quasars in Section 4, and put them in the context of the  $R-L$  relation in Section 5. In Section 6 we summarize the paper. Throughout the paper we use a  $\Lambda$ -dominated flat cosmology with  $H_0 = 70 \text{ km s}^{-1} \text{ Mpc}^{-1}$ ,  $\Omega_m = 0.3$ , and  $\Omega_\Lambda = 0.7$ . All magnitudes are on the AB system.

## 2. QUASAR SAMPLE

In this section we present the selection of our quasar sample. Before we go into the detailed steps, we briefly introduce the telescope and instrument that we used for the IBRM project, which is directly related to our sample selection. The telescope that we used is the Steward Observatory 2.3m Bok telescope, and the instrument is its prime focus imager 90Prime. 90Prime has a large, square field-of-view (FoV) of roughly one degree on a side. It uses four 4K thin CCDs that were optimized for U-band imaging (Zou et al. 2015). We used two broad-band filters  $i$  and  $z$ , and three intermediate-band filters, BACT12, BACT13, and BACT14. These intermediate-band filters were originally designed for the Beijing-Arizona-Taipei-Connecticut (BATC) Color Survey (e.g. Fan et al. 1996; Yan et al. 2000; Zhou et al. 2001). The broad-band filters are used to measure continuum flux. The effective wavelengths of the three intermediate-band filters are 8045, 8505, and 9171 Å, with the FWHMs of 230, 180, and 264 Å, respectively. They cover three wave-

length ranges with relatively weak OH sky emission, so imaging in these bands is very efficient.

### 2.1. Sample Selection

Our sample selection began with the SDSS DR7 quasar catalog delivered by Schneider et al. (2010) and Shen et al. (2011). The emission lines used for our IBRM project are  $H\alpha$  and  $H\beta$ , two of the strongest lines in quasar spectra. We first selected quasars at certain redshifts so that their  $H\alpha$  or  $H\beta$  emission lines are located in one of the three intermediate bands (the center of an emission line is roughly within the central 50% of the filter.) Specifically, the redshift ranges considered here are [0.216, 0.236], [0.290, 0.302], [0.385, 0.410], [0.642, 0.668], [0.741, 0.758], and [0.870, 0.904], and there are 4326 quasars in these redshift ranges. We then selected quasars in a certain coordinate range, because the observations of our IBRM project shared the Bok nights with the SDSS-RM project (Shen et al. 2015a), as we will see in the next section. The coordinate range chosen here is  $8\text{h} < \text{R.A.} < 13\text{h}$  and  $\text{Decl.} > 25 \text{ Deg}$ , and 1227 quasars passed this selection. We further selected targets in a certain brightness range (namely,  $17 < i < 19.5 \text{ mag}$ ) with high  $H\alpha$  or  $H\beta$  EW. The  $H\alpha$  and  $H\beta$  EW values were measured from the SDSS spectra and taken from Shen et al. (2011). We required that the observed  $H\alpha$  EW was greater than 180 Å, or the observed  $H\beta$  EW was greater than 90 Å. This ensures that the line emission contributes a significant fraction of the total flux in the intermediate bands. This is one of the keys for the success of this program. The choice of  $i < 19.5 \text{ mag}$  was to ensure that we can get high SNRs in the intermediate bands with 5 min integration time. The choice of  $i > 17 \text{ mag}$  was to select quasars with expected time lags (in the observed frame) shorter than the duration of our observing campaign (roughly 5–6 months). The expected time lags for most of the selected quasars are between 20 and 60 days. The observed-frame time lags also depends on redshift due to the time dilution of  $1 + z$  and the strong dependence of the intrinsic luminosity on redshift for a given apparent magnitude. Therefore, for very bright quasars at relatively high redshifts ( $z \geq 0.6$ ), their expected time lags could be significantly longer and even close to the duration of our RM campaign. We selected 622 quasars in this step.

After we obtained the list of the quasars from the above steps, we chose the area/fields that have more than one quasar per square degree (the FoV of the 90Prime). This was to increase the efficiency of the project. Meanwhile, we matched the quasars to the Pan-STARRS1 (PS1; Schlafly et al. 2012; Tonry et al. 2012; Magnier et al. 2013) preliminary catalog, and obtained their variability values as follows. For each quasar, we extracted the standard deviations of the magnitudes from the catalog. There are five standard deviation values for five PS1 bands ( $g_{P1}$ ,  $r_{P1}$ ,  $i_{P1}$ ,  $z_{P1}$ , and  $y_{P1}$ ), and we took the average of the second and third largest standard deviation values as the variability of this quasar. We then eliminated  $\sim 10\%$  of the sources whose variability was roughly consistent with error bars. Finally, from the remaining sources we selected 13 quasars or 5 fields for the IBRM project, by considering the following: 1) the fields are roughly evenly distributed between 8h and 13h for

**Table 1**  
Quasar Sample

ID	R.A. (J2000)	Decl. (J2000)	Redshift	$i$ (mag)	Line	EW	Filter
F1a	09:00:45.293	+33:54:22.38	0.228	17.93	H $\alpha$	205	BATC12
F1b	09:01:56.250	+33:33:49.49	0.878	19.00	H $\beta$	71	BATC14
F2a	09:46:59.593	+29:32:51.13	0.387	18.58	H $\alpha$	606	BATC14
F2b	09:50:46.582	+29:38:26.90	0.233	18.20	H $\alpha$	299	BATC12
F3a	11:27:59.260	+36:02:07.00	0.667	18.42	H $\beta$	132	BATC12
F3b	11:29:56.532	+36:49:19.24	0.398	19.05	H $\alpha$	563	BATC14
F3c	11:31:14.956	+36:02:38.30	0.229	18.22	H $\alpha$	263	BATC12
F4a	11:45:53.152	+28:13:13.41	0.401	18.73	H $\alpha$	230	BATC14
F4b	11:46:34.914	+28:26:41.96	0.225	18.11	H $\alpha$	249	BATC12
F4c	11:49:36.368	+27:44:04.83	0.748	18.95	H $\beta$	192	BATC13
F5a	12:36:35.259	+45:02:08.06	0.401	18.74	H $\alpha$	353	BATC14
F5b	12:36:58.110	+45:53:54.46	0.235	18.12	H $\alpha$	433	BATC12
F5c	12:38:42.730	+45:18:24.73	0.229	17.34	H $\alpha$	292	BATC12

**Note.** — The table lines separate five different fields. Column 7 shows the observed-frame EW values in units of  $\text{\AA}$ .

the convenience of observations; 2) the quasars have relatively strong H $\alpha$  (or H $\beta$ ) EWs (stronger are better); 3) the quasars show relatively strong variability. When the demands for 2) and 3) are difficult to meet simultaneously, we slightly favored 2), because quasar variability is a stochastic process.

Table 1 lists the details of the 13 quasars. Column 1 shows the ID of the quasars. We use ‘F1’ to ‘F5’ to denote the five fields, and use ‘a’ to ‘c’ to denote the quasars within a field. The following four columns are the coordinates, redshifts, and  $i$ -band magnitudes drawn from the SDSS DR7 catalog. Columns 6 and 7 shows the emission lines that we used and their EWs in the observed frame. Column 8 shows the intermediate filters that cover the lines. These quasars covers a redshift range of  $0.22 < z < 0.88$ . We mainly use the H $\alpha$  line (10 out of 13 quasars), because the H $\alpha$  line is much stronger than the H $\beta$  line, and thus quasars with strong H $\alpha$  were preferentially selected. Note that the EW of F1b is lower than our selection criterion. This is because the line is close to the red end of its SDSS spectrum, and the EW value given by the SDSS DR7 is not accurate. The value given in the table was measured from an MMT spectrum with much better quality (see the next subsection). The contributions of line emission to the intermediate-band fluxes are roughly between 35% and 70% for all objects except F1b, for which the line contribution is only  $\sim 20\%$ .

## 2.2. Optical Spectra

Single-epoch quasar optical spectra are needed to accurately derive the line contribution to the broad-band photometry. These quasars have optical spectra from SDSS I and II. The SDSS spectra do not cover the wavelength range beyond  $\sim 9100 \text{\AA}$ , which is needed for the BATC14 filter. For the quasars observed with the BATC14 filter (see Table 1), we obtained new optical spectra using the MMT Red Channel spectrograph. The observations were carried out as backup targets during other programs in 2014, when weather conditions were poor. The observations were made in long-slit mode with a spectral resolution of  $\sim 10 \text{\AA}$ . The integration time was roughly 5–10 min per object, which is sufficient for our purposes. The

spectra were reduced using standard IRAF routines<sup>7</sup>. The MMT spectra cover a wavelength range of  $7000\text{--}10000 \text{\AA}$ . The final spectra of these quasars are the combination of the SDSS and MMT spectra.

Figure 1 shows the optical spectra of our quasar sample in the observed frame. As we mentioned above, some spectra were directly taken from the SDSS, while the others were the combination of the SDSS and MMT spectra. In each panel of Figure 1, we also show the transmission curves of the 90Prime  $i$  and  $z$  filters (the blue dotted profiles) and one of the intermediate filters (the red dotted profile) that covers H $\alpha$  or H $\beta$ . The CCD quantum efficiency has been taken into account. Note that the transmission curves of the 90Prime  $i$  and  $z$  filters are slightly different from those of the SDSS  $i$  and  $z$  filters.

In several cases, the intermediate bands do not entirely cover the emission lines (e.g. F2a and F5b). The effect of missing line wings on the measurement of BLR sizes is very small. When we calculate line emission for light curves in section 4, we only consider the contribution from the part covered by the intermediate bands, which contains more than 90% (in most cases more than 95%) of the total line flux. Pozo Nuñez et al. (2014) conducted detailed calculations to estimate the consequences of the above missing line wings on photometric RM results, and concluded that the effect on the measurements of BLR sizes is only a few per cent. This is negligible compared to the size measurement uncertainties we will get in section 4.

## 3. OBSERVATIONS AND DATA REDUCTION

The IBRM project was carried out in the spring semester, 2014. It shared the Bok nights with the SDSS-RM project. As we mentioned earlier, the SDSS-RM project was one of the SDSS III ancillary projects. It used the CFHT and Bok telescopes to do broad-band ( $g$  and  $i$ ) photometry for measurements of continuum light curves in SDSS-RM (Shen et al. 2015a). Our targets and observing time were coordinated with the SDSS-RM project.

<sup>7</sup> IRAF is distributed by the National Optical Astronomy Observatory, which is operated by the Association of Universities for Research in Astronomy (AURA) under cooperative agreement with the National Science Foundation.

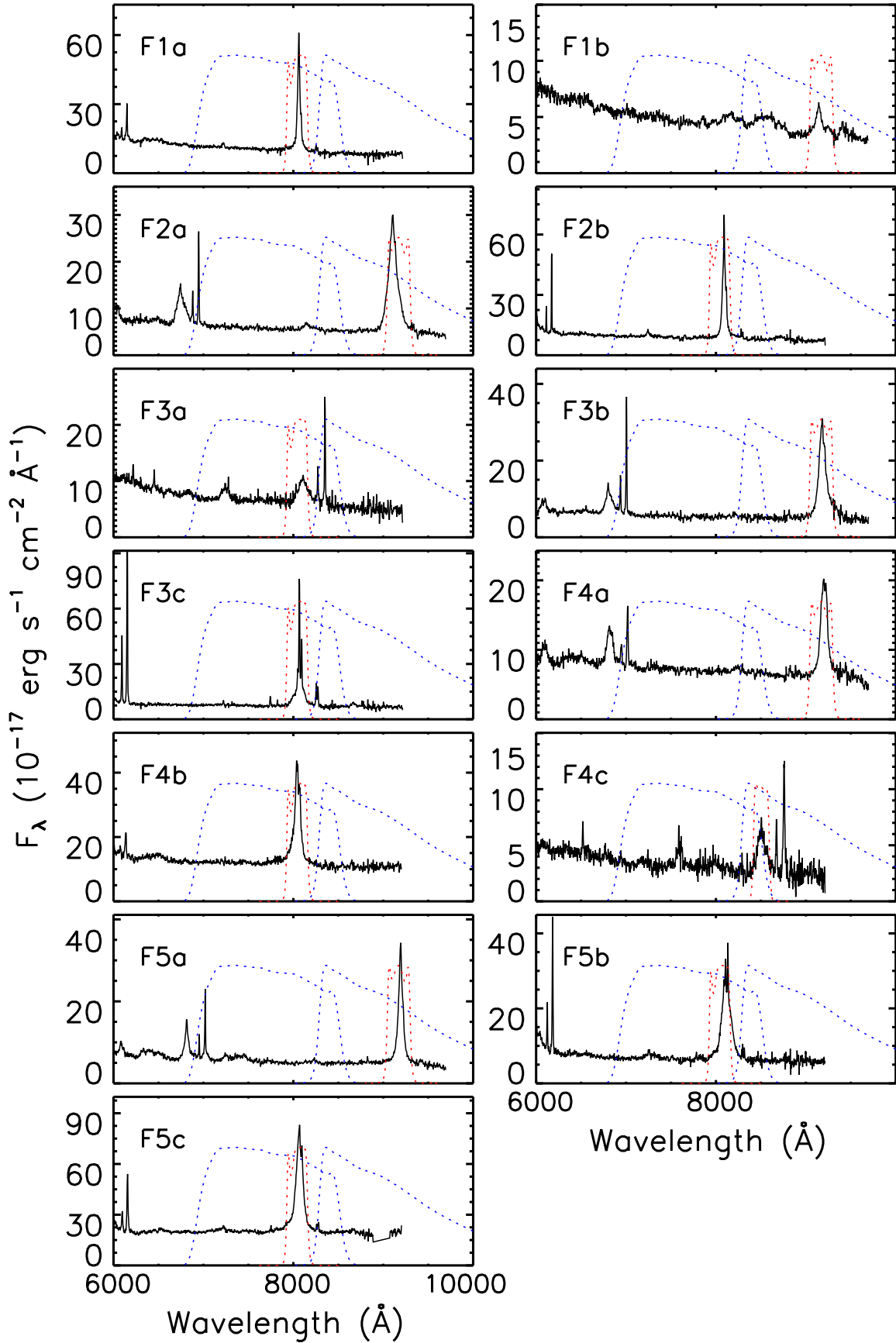


**Figure 1.** Observed-frame optical spectra of the 13 quasars in our sample. The spectra were taken from the SDSS and the MMT. The blue dotted profiles represent the transmission curves of the 90Prime *i* and *z*-band filters, and the red dotted profiles represent three intermediate filters that covers H $\alpha$  or H $\beta$ . The CCD quantum efficiency has been taken into account, and the curves have been normalized so that their peak values are the same.

### 3.1. Bok Observations

The Bok observations of the quasars were conducted in January through June, 2014. Due to the constraints from the telescope scheduling, we obtained one or two long observing blocks each month (see section 4.1). Hence the Bok nights for the SDSS-RM and IBRM projects were not evenly distributed, and were clustered around the nights with relatively bright moon phase. Such an observing schedule does not provide an optimal cadence for RM studies. Each of the five fields were observed for between 20 and 30 epochs over the full campaign.

Because of the large FoV of the 90Prime, the 13 quasars in our sample were covered by only 5 telescope pointings or fields from F1 to F5. We usually observed at least 3 fields per epoch/night. The observations were made via observing scripts. Each time after we slewed the telescope to a new field, the scripts automatically changed filters, tweaked focus, and took the data, in the order of  $i$ ,  $z$ , BATC12, BATC14 (and BATC13 for Field 4). The typical on-source integration time was 150 s in the  $i$  band, and 300 s in the other bands. The observing conditions were mostly moderate with clear skies, moderate seeing ( $\sim 1.5''$ ), but significant moonlight.

### 3.2. Data Reduction

The 90Prime images were reduced in a standard fashion using our own IDL routines. The basic procedure was described in Jiang et al. (2015). First, we made a master bias image and a master flat image from bias and flat images taken in the same night. A bad pixel mask was also created from the flat image. Science images were then overscan and bias-corrected and flat-fielded. Next we identified saturated pixels and bleeding trails, and incorporated them (along with the bad-pixel mask) into the weight images. The affected pixels were interpolated over in the science images. We call the science images at this stage ‘corrected images’.

The 90Prime CCDs are thin chips, and thus produce strong fringing in the bands that we used. We subtracted sky background and fringes using two iterations. The first-round of sky subtraction was performed by fitting a low-order 2D polynomial function to the background. A master fringing image (per filter) was made by median stacking at least eight sky-subtracted images in the same filter. This fringing image was scaled and subtracted from the original ‘corrected’ images (before sky-subtraction was done). We detected objects in the fringe-subtracted images using **SExtractor** (Bertin & Arnouts 1996). A better sky image was produced from each fringe-subtracted image with the detected objects masked out. Then the second round of sky and fringe subtraction was performed, but with the detected objects masked out.

In order to derive astrometry, we detected bright objects using **SExtractor** (Bertin & Arnouts 1996), and calculated astrometric solutions using **SCAMP** (Bertin 2006) by matching objects to the SDSS. With the new astrometry we re-mapped the images using **SWARP** (Bertin et al. 2002). The re-mapped images have a native pixel size of  $0.455''$ .

### 3.3. Photometry

Accurate (relative) photometry is another key for the success of this project. In order to achieve accurate photometry, for any given quasar in the whole observing campaign, we used a large number of nearby bright point sources for photometric calibration. These bright sources and our quasar targets was always located in roughly the same part of the same CCD, which minimizes the effect from any large-scale systematics. This allows us to achieve relatively small uncertainties ( $\sim 0.01$  mag) on the magnitude zero points that are usually negligible compared to the uncertainties in the light curves that we derive in Section 4. The details are as follows.

The four CCDs were read out via 16 amplifiers, with 4 amplifiers per CCD. For any of the 13 quasars in an image, we only performed photometry for the amplifier area in which this quasar was located (roughly  $15'$  on a side). We did not use other parts of the image (for this quasar) due to the possible small zero point shift across the amplifiers and CCDs (Zou et al. 2015).

We first chose a ‘standard’ night, which was photometric and relatively dark, and performed photometry for the images taken in this standard night. Photometry was measured within an aperture (diameter) size of 8 pixels ( $\sim 3''.6$ ) using **SExtractor**. We then picked up bright (at least  $30\sigma$  detection) but unsaturated point sources, and matched them to the SDSS. The density of the bright stars is about 50–100 per amplifier. We used the SDSS PSF magnitudes, so the measured magnitudes are total magnitudes with aperture corrections automatically taken into account. After we obtained the  $i$  and  $z$ -band magnitudes for a given object, we calculated its intermediate-band magnitudes as follows. We assumed that its spectrum in the wavelength range of the  $i$  and  $z$  bands (also covers the three intermediate bands) was a power law, which is determined by its  $i$  and  $z$ -band magnitudes. Then its intermediate-band magnitudes were directly calculated from this power-law spectrum and the intermediate-band transmission curves. The resultant magnitudes have very weak dependence (usually  $\Delta m \leq 0.03$  mag) on the assumption of the spectrum shape, as long as there are no emission or absorption lines in the intermediate bands. Such small uncertainties on the zero magnitude points have no effect on our measurement of light curves, which rely on relative photometry. We calculated AB magnitudes for all these bright stars taken in the standard night. These bright stars were used as standard stars for all other images.

We then measured photometry for the images taken in all other nights. The procedure was the same. But we used the bright stars found in the standard night as ‘standard stars’, and used their magnitudes for absolute flux calibration. Because of the large numbers of bright standard stars for any given quasar, we achieved high accuracy on relative zero flux points. Figure 2 illustrates this point. Its horizontal axis shows the magnitude difference of the standard stars taken between the standard night and the first several nights other than the standard night. The vertical axis shows the distributions of the magnitude difference. The sigma values quoted in the figure were estimated by fitting a Gaussian profile to the top 80% of the distributions. The bottom 20% deviates from the Gaussian distribution, likely due to some unreliable ‘standard’ stars, such as variable stars. The tight distributions of the magnitude difference in the

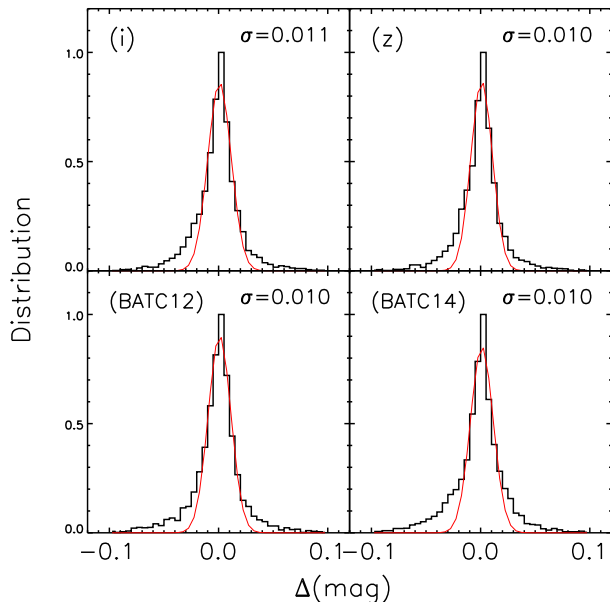


**Figure 2.** Accuracy of the flux calibration. The horizontal axis shows the magnitude difference of the standard stars taken between the standard night and the first several nights other than the standard night. The vertical axis shows the normalized distribution of the magnitude difference. The standard deviation ( $\sigma$ ) values were estimated by fitting a Gaussian profile (the red profiles) to the top 80% of the distributions (the bottom 20% significantly deviates from the Gaussian distribution). The tight distributions in the four bands suggest that our flux calibration is very accurate.

four bands suggest that our accurate flux calibration is about 0.010 mag rms. We did not plot the distribution in BATC13, which is similar to those in the other 4 bands.

Figure 3 shows the measurement uncertainties as a function of total magnitude in 4 bands for all quasars observed in the whole RM campaign. The errors are estimated within an aperture (diameter) size of 8 pixels from **SExtractor**. The uncertainties from the absolute flux calibration are not included in this plot. In our images, the noise is completely dominated by sky background, so these errors are quite reliable (background variance reflects errors). The errors are mostly smaller than 0.02 mag. In rare cases errors can be larger than 0.05 mag, mostly caused by low sky transparency.

The final photometric errors take into account (quadratically) the measurement errors (Figure 3), the errors from the flux calibration (Figure 2), and the uncertainties due to varying seeing. A quasar host galaxy is not a point source, and its radial profile is broader than PSF, so the aperture correction derived from point sources does not precisely correct for all light loss. This results in photometric variation with varying seeing. We estimate this variation as follows. In section 5.1, when we measure the host galaxy contribution for each quasar, we generate a combined image (from single-epoch images with good seeing), build a PSF model image, and derive a host-galaxy image using image decomposition. We make use of these ‘deep’ and model images, because single-epoch images do not have sufficient SNR. We convolve these images with Gaussian kernels, which mimics varying seeing. We then perform aperture photometry in the same manner as in single-epoch images. The only difference is that the aperture correction is measured from the corresponding PSF images. We find that when PSF

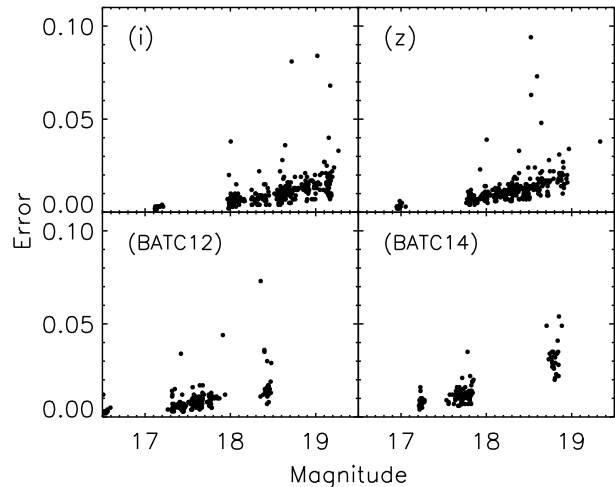


**Figure 3.** Measurement uncertainties as a function of total magnitude for all quasars observed in the whole RM campaign. The errors are measured within an aperture (diameter) size of 8 pixels. The uncertainties from absolute flux calibration are not included. The errors are mostly smaller than 0.02 mag. In rare cases, errors can be larger than 0.05 mag caused by low sky transparency.

varies from  $\sim 1.2''$  to  $\sim 1.8''$  (almost covers our seeing range), the photometric variation is about  $0.007 \pm 0.002$  mag. Such variation is small for our targets, partly because we used a large aperture for photometry. In many cases, however, it is comparable to the measurement errors shown in Figure 3. Thus we carry this error of 0.007 mag to the final photometric errors.

#### 4. TIME LAGS

In this section we present our main results. For each quasar in Table 1, we first compute the continuum and emission line light curves. This step is straightforward, as we have decent optical spectra and accurate broad- and intermediate-band photometry. We then derive the time lag between continuum and line emission in standard ways.

##### 4.1. Light Curves

For each quasar we have a single-epoch optical spectrum and a series of  $i$ ,  $z$ , and intermediate-band photometric measurements. We first calculate the contribution of the line emission (or equivalently the contribution of the continuum emission) to the broad-band photometry using the optical spectrum. We select regions with little line emission in the spectrum as continuum windows, and fit a power-law curve ( $f_\lambda = b \times \lambda^\alpha$ ) to these windows. This power-law continuum may contain a central AGN component and a host galaxy component (see the next section). As long as the host galaxy does not vary (a constant component), the inclusion of the host galaxy component does not affect the determination of time lags. The line emission is obtained by subtracting the power-law continuum from the spectrum. We assume that the contribution of the line emission to the broad-band photometry does not vary with time. The reason is that the line contribution is smaller than 5%, and the line variability is usually smaller than 20%, so the effect of line variability on broad-band photometry is smaller than 1%. As we will see below, the continuum value we derive for a quasar is determined by two broad bands ( $i$  and  $z$ ), with one band without line contamina-

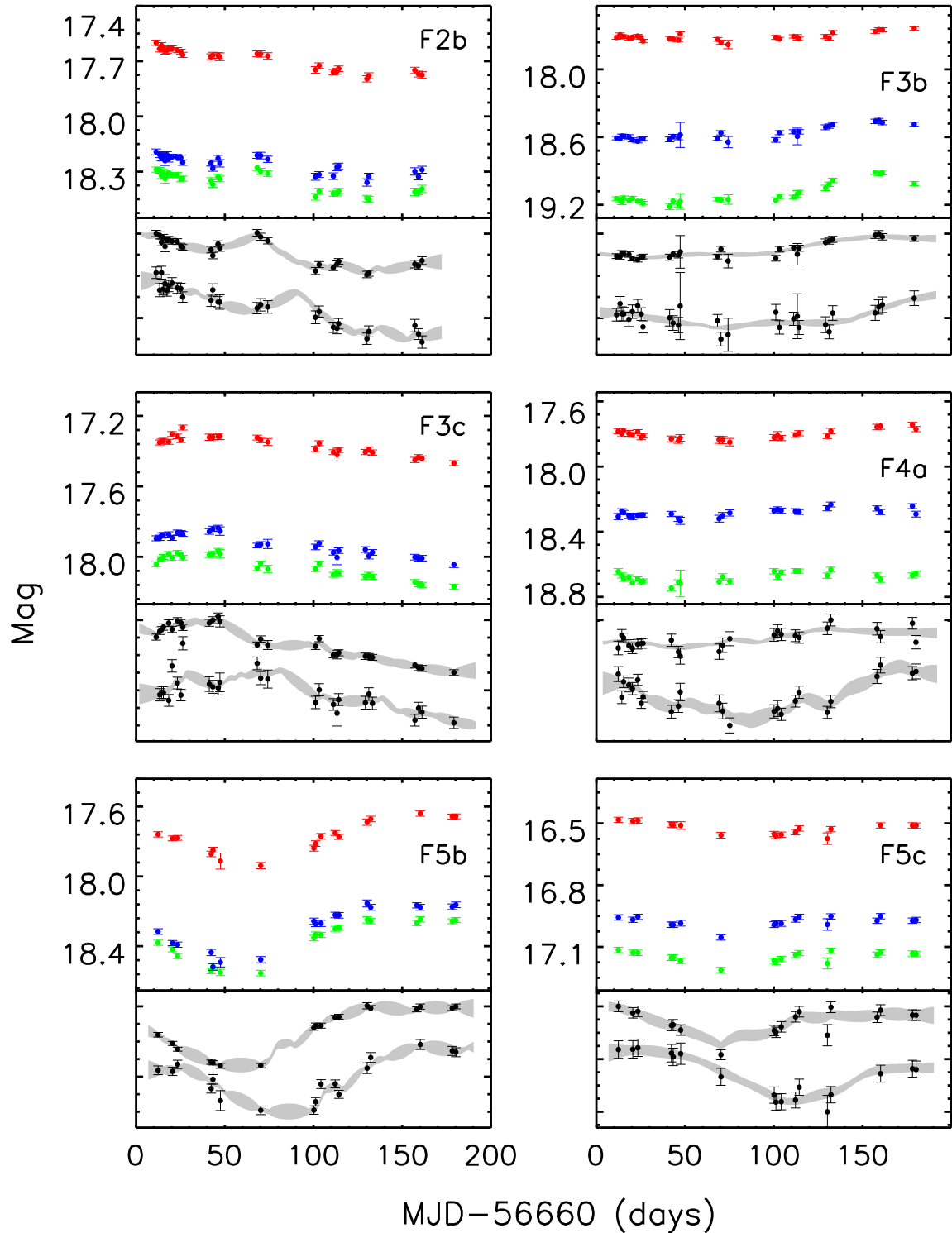


**Figure 4.** Light curves of the 6 quasars that show significant time lags during our IBRM campaign. For each object in the upper panel, the blue and green circles show the light curves in the  $i$  and  $z$  bands, and the red circles indicate the light curve in the intermediate band. The lower panel shows the light curves of the continuum flux (upper curves) and line flux (lower curves). See section 4.1 for details on how the line and continuum flux is derived. These two curves have been shifted along the y axis so that they are displayed clearly. The gray shaded curves indicate the simulated light curves ( $1\sigma$  area) as computed from JAVELIN (section 4.1).

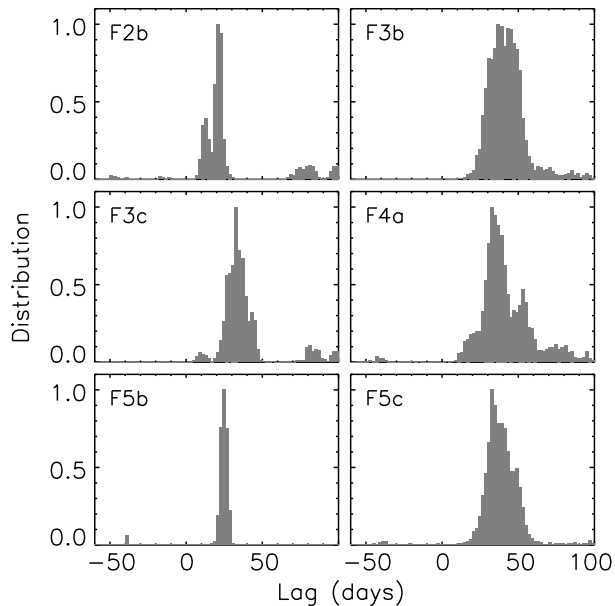


**Figure 5.** Time lags (in the observed frame) for 6 quasars with significant lag detections. The lag distribution for each quasar is based on 10,000 experiments using JAVELIN (Zu et al. 2011). See section 4.2 for details. The distributions have been normalized so that the peak values are equal to 1.

tion, so the effect of line variability on continuum is even smaller by roughly a factor of two, which is much smaller than the uncertainties in the light curves derived below. Thus our above assumption has a negligible effect on the measurement of the continuum, but largely simplifies our procedure.

We then derive the line flux and continuum flux at the wavelength of the intermediate band from their corresponding  $i$ ,  $z$ , and intermediate-band photometry at each epoch. The continuum components at  $i$  and  $z$  are computed by subtracting the line contribution from these bands. A power-law continuum is derived analytically from the two flux measurements at the effective wavelengths of the  $i$  and  $z$  bands. We then determine the continuum value at the effective wavelength of the intermediate-band from the power-law continuum. This continuum value is the continuum that will be used for light curves. Finally the line emission is obtained by subtracting the continuum component from the intermediate-band photometry. Figure 4 plots the light curves of the 6 quasars that show significant time lags during our IBRM campaign (see the next subsection). For each object, the upper panel shows the light curves in the  $i$  (blue circles),  $z$  (green circles), and one of the intermediate bands (red circles). The lower panel shows the light curves of the continuum flux (upper curves) and line flux (lower curves).

#### 4.2. Lag Measurements

We estimate time lags between the line and continuum emission derived above using the JAVELIN package (Zu et al. 2011, 2013). As we have seen, the light curves were unevenly (sometimes sparsely) sampled, due to the constraints from telescope time scheduling. JAVELIN is able to deal with such an uneven sampling. It assumes that the variability of a quasar/AGN can be well described by the damped random walk (DRW) model

**Table 2**  
Time Lags and Luminosities of the 6 Quasars

ID	Redshift	Lag (days)	$\text{Log}(\lambda L_\lambda)$	$f_{\text{host}}$
F2b	0.233	$21.1^{+46.9}_{-8.3}$	43.84	0.21
F3b	0.398	$41.2^{+9.8}_{-9.9}$	44.17	0.19
F3c	0.229	$34.0^{+9.7}_{-6.5}$	43.84	0.37
F4a	0.401	$38.1^{+17.8}_{-9.1}$	44.32	0.28
F5b	0.235	$25.0^{+2.2}_{-2.3}$	43.79	0.22
F5c	0.229	$37.9^{+10.3}_{-7.4}$	44.25	0.36

**Note.** — The time lags are in the observed frame. The quasar luminosities (in units of  $\text{ergs}^{-1}$ ) have been corrected for host-galaxy contamination. The last column shows the contribution from host galaxies (section 5.1).

(e.g. Kelly et al. 2009), and its emission line light curve is the lagged and scaled version of its continuum light curve. For a given quasar, we first model its continuum variability using JAVELIN, and find the distribution of the DRW parameters. We then statistically interpolate the continuum light curve. The light curve is shifted, smoothed, and scaled, before it is compared to the corresponding emission-line curve. The smoothing here refers to the use of a transfer function (non-Delta-function) in JAVELIN to mimic the realistic line response to continuum light curves. This is due to the fact that the BLR clouds are distributed at different radii with different velocities, which results in a transfer function that is broad in lag. For details, see the JAVELIN papers (Zu et al. 2011, 2013). This process is performed 10,000 times using the MCMC method. The final results are the best model fits for each try. Note that all calculations above are based on flux (not magnitudes).

Based on the time lag measurements from JAVELIN, we find that 6 (out of 13) quasars in our sample show clear lag detections during our IBRM campaign (we will discuss the other quasars in the next subsection). The lag range allowed in the above calculation is from  $-100$  to  $+100$  days. We do not consider a wider range, simply because the duration of the IBRM campaign was only 150–170 days. Figure 5 shows the distributions of the measured lags for the 6 quasars (their light curves are shown in Figure 4). They show clear single distribution peaks. The results are listed in Table 2. The lag errors in the table are calculated by including 16% and 84% of the total distributions around the median distribution (50% of the total). Obviously they depend on the lag range that we consider. On the other hand, they are not sensitive to the lag range, as long as the lag detections are substantial with most distributions clustered around the median values. This applies to all quasars except F2b in Figure 5. The lag measured for F2b is  $21^{+47}_{-8}$  days. It has a large upper error due to the non-negligible fraction of the total distribution beyond 70 days. If we were to reduce the lag range to  $-100 \sim 70$ , the lag becomes  $21^{+2}_{-7}$  days, with a much smaller upper error. We adopt the larger error for consistency in the paper.

We further use the discrete correlation function (DCF) to validate the above lag detections. The algorithm we adopt is the  $z$ -transformed DCF (zDCF), which was designed to handle unevenly sampled light curves (Alexander 2013). The estimated DCFs for the 6 quasars



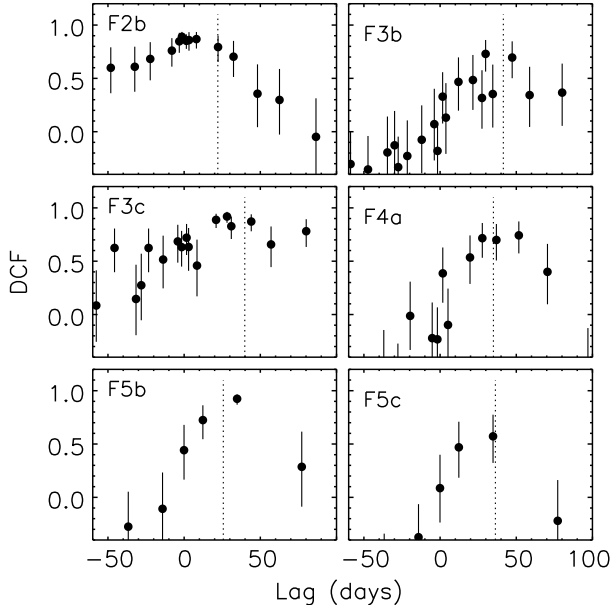


**Figure 6.** DCFs for the 6 quasars with significant lag detections (in the observed frame). The DCFs are estimated using the zDCF (Alexander 2013). The dotted vertical lines indicate the lags measured from JAVELIN (Table 2 or Figure 5). The results from the zDCF and JAVELIN are consistent.

are shown in Figure 6. These quasars also show clear DCF peaks. The lag uncertainties from the zDCF are larger. One reason is that the zDCF uses time-lag bins, and the minimum number required in each bin is roughly 11 for meaningful statistics in the zDCF. Given the small numbers of epochs in our IBRM project, the zDCF can only coarsely sample the light curves in the lag time space. Nevertheless, the zDCF peaks in Figure 6 are consistent with the results from JAVELIN except for F2b. F2b shows a significant lag detection by JAVELIN in Figure 5, but its zDCF peaks at  $\sim 0$ . The lag detection from JAVELIN could be real, or a false positive because of the sparse-sampling in light curves. On the other hand, the zDCF of F2b is broad, which is not against a lag of  $\sim 20$  days. This can be solved with more evenly and finely sampled light curves in the future.

We perform a simple experiment to test our results. For any pair of light curves (continuum and line) in the 6 quasars, we randomly re-order one curve, and repeat the above processes using JAVELIN to estimate the rate of false positives. This is done a hundred times for each quasar (each pair of light curves). These tests generally show small false positive rates. For the first four quasars that were observed in nearly 30 epochs, the false positive rates are only 3–4%. The rates increase to 7–9% for the last two quasars that were observed only  $\sim 20$  times (see Shen et al. (2015b) for a detailed discussion).

The detected lags in the 6 quasars are all for  $H\alpha$ , and at relatively low redshifts between 0.22 and 0.40. It is not surprising, because 10 out of the 13 lines in the original sample are  $H\alpha$ , and  $H\alpha$  is much stronger than  $H\beta$  on average. In addition, higher redshifts usually mean higher intrinsic luminosities and larger time dilution ( $1+z$ ), leading to much larger observed time lags that are likely beyond the detection capability of our IBRM campaign.

#### 4.3. Quasars without Significant Lag Detections

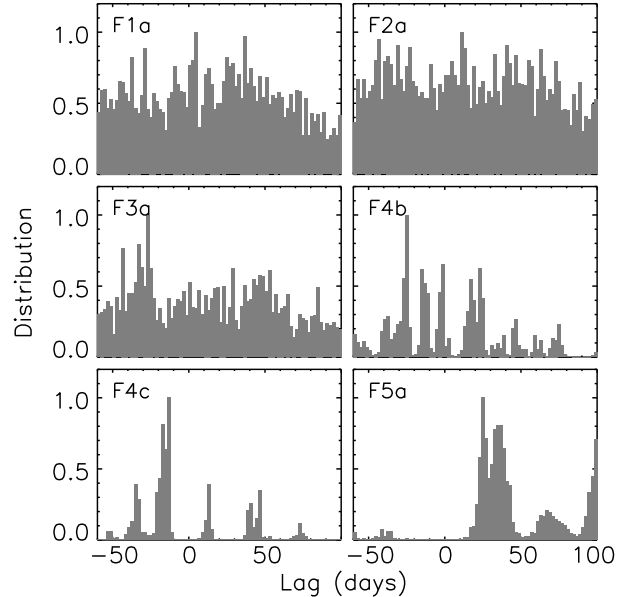


**Figure 7.** Distributions of the time lags derived from JAVELIN for 6 of the 7 quasars without obvious lag detections. The distributions have been normalized so that the peak values are equal to 1.

We did not detect time lags between continuum and line emission in the other 7 quasars in our sample. Similar to Figure 6, Figure 7 shows the distributions of the lags for these quasars from JAVELIN. Unlike those in Figure 6, quasars in Figure 7 do not show single strong peaks. They rather show multiple peaks or continuous distributions. There are two main reasons for these non-detection. The first reason is that the expected time lags based on the current  $R-L$  relation (e.g. Bentz et al. 2013) are comparable to the duration of our campaign. For example, the lags expected for F1b, F3a, and F4c are greater than 120 days, primarily due to their high redshifts. The second reason is that the variability is small, or that the light curves are relatively flat. These quasars show moderate to large variability in the PS1 data. But quasar variability is a stochastic process, and past large variability does not guarantee large variability in the future. In addition, large gaps in light curves can often cause aliasing, and it seems the case for F4c. For these objects, our data were insufficient to detect lags.

## 5. BLR SIZE-LUMINOSITY RELATION

### 5.1. Light from Host Galaxies

Quasar host galaxies may contribute a significant fraction of the total light in the bands that we measured. There are two general methods to estimate the light from the hosts: image decomposition and spectral decomposition. We do not have the high SNR spectra that spectral decomposition requires (e.g. Shen et al. 2015c), so we rely on image decomposition. Image decomposition works better on images with better PSFs (or seeing). The site of the Bok telescope does not deliver good seeing, and the average PSF size of our images is about  $1.5''$ . In order to construct a deep combined image with a decent PSF for each quasar, we choose 50% of the  $i$ -band images with the best PSF sizes, and co-add them to a stacked image. The reason to choose the  $i$ -band is twofold. One is that it is the deepest band. The other one is that

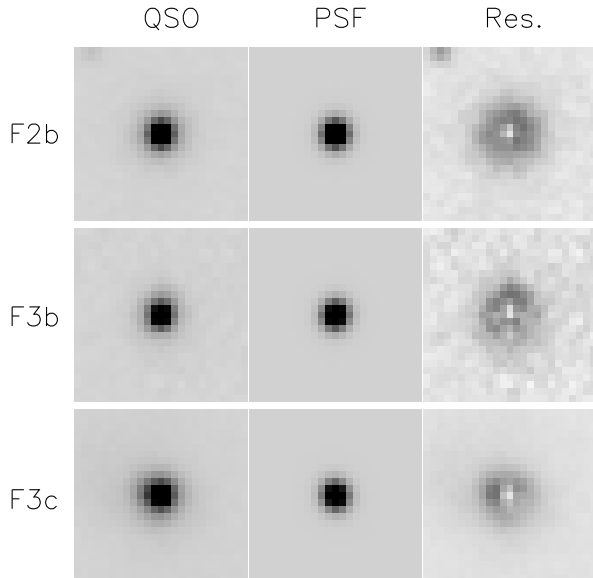


**Figure 8.** Examples for image decomposition. We show the first 3 of the 6 quasars with lag detection. For each quasar, the first column shows the combined  $i$ -band stamp image, with the quasar well centered in the middle. The middle column shows the PSF image constructed from the combined image. The third column is the residual image or the host galaxy component after the PSF image is scaled and subtracted from the quasar image. The quasar and PSF images have the same intensity scale. The residual images have a different intensity scale.

its effective wavelength is close to the rest-frame  $5100 \text{ \AA}$  (the commonly used wavelength) for our quasars. As for flux calibration, we only consider  $1/16$  of the image, i.e., the amplifier that the quasar is located in. This is to avoid any possible large PSF variation across the large FoV. The PSF sizes of the combined images are about  $1.1''$ , which is good enough for image decomposition on low-redshift quasars (e.g. Matsuoka et al. 2014).

We perform image decomposition on the combined  $i$ -band images. For each quasar/image, the detailed steps are as follows. We first derive a PSF model for the quasar using PSFex (Bertin 2011). PSFex finds point sources in the image, and builds PSF models as a function of position. We take the PSF model that is closest to the quasar position as the PSF model for the quasar, although the PSF variations are quite small across a single amplifier in our images. The PSF image size is 25 pixels on a side, with the peak pixel centered in the middle. We then calculate an accurate central position for the quasar in the image, and re-sample the image to produce a stamp image centered on the quasar. The size of the stamp image is also  $25 \times 25$  pixels. Following Matsuoka et al. (2014), we assume that the central pixel (peak value) of the quasar image is completely dominated by the quasar/AGN component. Under this assumption, we scale the PSF and subtract it from the quasar image. The residual is referred to as the host galaxy component. Figure 8 demonstrates the procedure by showing three quasars.

From the above procedure, the fraction of the AGN (or host) component is simply calculated by doing aperture photometry on the PSF image and the quasar image. In our 6 quasars, the host contribution is roughly between 19% and 37%. In order to measure the luminosity of an

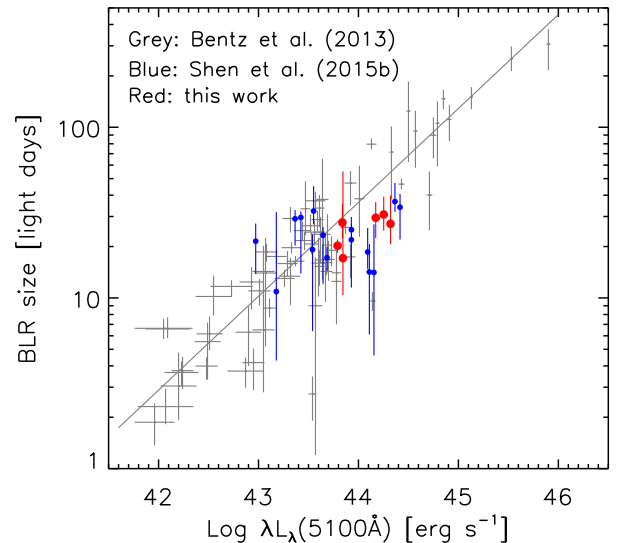


**Figure 9.** The BLR size-luminosity relation in rest frame. The gray symbols represent the current  $R-L$  relation from successful RM campaigns compiled by Bentz et al. (2013). The blue circles represent recent results from SDSS-RM (Shen et al. 2015b). Our results are shown as the red circles, and are roughly consistent with the previous results.

AGN at the rest-frame  $5100 \text{ \AA}$ , we scale its spectrum in Figure 1 to match the mean of the  $i$ -band magnitudes obtained in IBRM. We then calculate the AGN luminosity from the spectrum after removing the host contribution. The absolute values of the AGN luminosities are listed in Table 2.

## 5.2. $R-L$ Relation

The relation between the BLR size and quasar luminosity provides the basis for determining SMBH masses in high-redshift quasars/AGN with single-epoch spectroscopy (for a recent review, see Shen (2013)). Accurate measurements of SMBH masses are particularly important in the context of the SMBH and host galaxy co-evolution (Kormendy & Ho 2013). The masses from RM can be calibrated from the local  $M_{\text{BH}} - \sigma_*$  relation (e.g. Ho & Kim 2015). Our sample is still small, and would not improve the  $R-L$  relation. On the other hand, the quasars in this sample are at relatively high redshifts, and thus may test the current  $R-L$  relation at  $0.2 < z < 0.4$ .

Figure 9 shows the current  $R-L$  relation from successful RM campaigns compiled by Bentz et al. (2013). Different emission lines have different ionization potentials, so the corresponding BLR sizes are different. The relation shown in Figure 9 was mostly built from  $\text{H}\beta$  measurements of local AGN. We also plot the recent results on  $\text{H}\beta$  and  $\text{Mg II}$  lags at  $z \geq 0.3$  (the blue circles) from the SDSS-RM project (Shen et al. 2015b). Our results for the 6 quasars with lag detections are shown as the red circles. They are roughly consistent with the  $R-L$  relation derived from local AGN. Our sample is primarily based on the  $\text{H}\alpha$  line, which has a shallower ionization potential compared to  $\text{H}\beta$ , and is thus expected to have a larger BLR size. However, the difference between the  $\text{H}\alpha$  lag and  $\text{H}\beta$  lag is unclear, and may depend on quasar luminosity. Several previous studies show that the difference ranges between 20% and 50% (e.g. Kaspi et al. 2000; Kollatschny 2003; Bentz et al. 2010; Haas et al. 2011). Given the scatter in the relation, our lag measurements

are still consistent with the previous results.

We note that our 6 quasars occupy a small part of the parameter space in Figure 9. This is due to the small sample size and the strong target selection bias. Our targets were selected to be bright, and they presumably have relatively large BLR sizes. If there were fainter quasars in our sample, we would not be able to detect their time lags (and thus they would not show up in Figure 9) because of the coarsely sample light curves. On the other hand, much more luminous quasars do not show up in the figure either, since these quasars have much longer time lags and cannot be detected in the IBRM duration, as we discussed in section 4.3. Therefore, the consistency of our results with previous studies does not mean that we have validated the current  $R-L$  relation at  $0.2 < z < 0.4$ . A larger, unbiased sample covering a much larger parameter space is needed.

## 6. SUMMARY AND FUTURE PROSPECTS

We have presented our IBRM program, a photometric RM program with broad and intermediate-band photometry. The intermediate bands that we chose are centered at 8045, 8505, and 9171 Å. They cover three wavelength ranges with relatively weak OH sky emission, thus imaging in these bands is very efficient. Our sample consists of 13 quasars at redshift between 0.2 and 0.9. These quasars were selected to have strong  $H\alpha$  or  $H\beta$  emission lines that are located in one of the intermediate-bands. The IBRM campaign was carried out with the 90Prime camera on the Bok telescope. The 90Prime has a large FoV and covered 13 quasars within five pointings/fields. The five fields were observed in the  $i$ ,  $z$ , and intermediate-bands in 20–30 epochs. These epochs were unevenly distributed in a duration of 5–6 months, so the cadence is not optimal for RM experiments. By using a large number of standard stars for each quasar, we achieved high accuracy on the photometric measurements. The combination of the broad and intermediate-band photometry allows us to precisely determine the light curves of the optical continuum and emission line. We detected significant time lags between continuum and line emission in 6 (out of 13) quasars in our sample. The time lags are consistent with the  $R-L$  relation derived from  $H\beta$  in low-redshift AGN.

Photometric RM with intermediate-band photometry has two major advantages. First, as with any implementation of photometric RM, it does not require spectroscopic observations, and can be easily performed with small telescopes. Second, the bandwidth of an intermediate filter is narrow enough that the line flux still contributes a significant fraction of the total flux in the band. Meanwhile, it is wider than narrow bands so that it is possible to include more than one target (at similar redshifts) per telescope pointing, which substantially increases observing efficiency.

Based on our experience from the IBRM program, we may increase our efficiency and improve our success rate in future RM campaigns with intermediate-band photometry. We plan to carry out a larger RM program using the Near-Earth Object Survey Telescope (NEOST) in Xuyu, China. NEOST is a 1m telescope with a FoV of  $9 \text{ deg}^2$ . With such a large FoV, we can monitor several (up to  $\sim 10$ ) quasars per telescope pointing. Our current IBRM experiment contains only 20–30 unevenly-

distributed epochs. We will make more observations (40–50 epochs) with better cadence, which will largely increase the success rate and improve time lag measurements. Ideally, we can complete this RM campaign for 100 quasars with 60 nights (45 epochs in 6 months) on the NEOST telescope.

We also plan to extend the baseline from 6 months to 18 months, with more sparse sampling after 6 months. This is to explore higher-redshift and higher-luminosity quasars. The maximum redshift that the three intermediate bands can reach for  $H\beta$  is roughly 0.9, which is much higher than the redshifts of the majority quasars shown in Figure 9. We will further extend this method other lines such as  $Mg \text{ II}$ , although RM with  $Mg \text{ II}$  is significantly more difficult because the line is generally much weaker than  $H\alpha$  and  $H\beta$ .

We acknowledge the support from a 985 project at Peking University, and the support from a Youth Qianren program through National Science Foundation of China. We would like to thank Y. AlSayyad, Y. Chen, K.D. Denney, S. Eftekharzadeh, Y. Gao, P.B. Hall, S. Jia, C.M. Peters, K. Ponder, J.A. Rogerson, R.N. Smith, and F. Wang for their help with the Bok observations. The Pan-STARRS1 Surveys (PS1) have been made possible through contributions of the Institute for Astronomy, the University of Hawaii, the Pan-STARRS Project Office, the Max-Planck Society and its participating institutes, the Max Planck Institute for Astronomy, Heidelberg and the Max Planck Institute for Extraterrestrial Physics, Garching, The Johns Hopkins University, Durham University, the University of Edinburgh, Queen’s University Belfast, the Harvard-Smithsonian Center for Astrophysics, the Las Cumbres Observatory Global Telescope Network Incorporated, the National Central University of Taiwan, the Space Telescope Science Institute, the National Aeronautics and Space Administration under Grant No. NNX08AR22G issued through the Planetary Science Division of the NASA Science Mission Directorate, the National Science Foundation under Grant No. AST-1238877, the University of Maryland, and Eotvos Lorand University (ELTE) and the Los Alamos National Laboratory.

*Facilities:* Bok (90Prime), MMT (Red Channel spectrograph), Pan-STARRS1

## REFERENCES

- Alexander, T. 2013, arXiv:1302.1508
- Barth, A. J., Nguyen, M. L., Malkan, M. A., et al. 2011, ApJ, 732, 121
- Barth, A. J., Bennert, V. N., Canalizo, G., et al. 2015, ApJS, 217, 26
- Bentz, M. C., Walsh, J. L., Barth, A. J., et al. 2009, ApJ, 705, 199
- Bentz, M. C., Walsh, J. L., Barth, A. J., et al. 2010, ApJ, 716, 993
- Bentz, M. C., Denney, K. D., Grier, C. J., et al. 2013, ApJ, 767, 149
- Bentz, M. C. 2015, arXiv:1505.04805
- Bertin, E., & Arnouts, S. 1996, A&AS, 117, 393
- Bertin, E., Mellier, Y., Radovich, M., et al. 2002, Astronomical Data Analysis Software and Systems XI, 281, 228
- Bertin, E. 2006, in ASP Conf. Ser. 351, Astronomical Data Analysis Software and Systems XV, ed. C. Gabriel, C. Arviset, D. Ponz, & E. Solano (San Francisco, CA: ASP), 112
- Bertin, E. 2011, Astronomical Data Analysis Software and Systems XX, 442, 435

- Blandford, R. D., & McKee, C. F. 1982, *ApJ*, 255, 419
- Chelouche, D., & Daniel, E. 2012, *ApJ*, 747, 62
- Chelouche, D., Shemmer, O., Cotlier, G. I., Barth, A. J., & Rafter, S. E. 2014, *ApJ*, 785, 140
- Denney, K. D., Peterson, B. M., Pogge, R. W., et al. 2009, *ApJ*, 704, L80
- Denney, K. D., Peterson, B. M., Pogge, R. W., et al. 2010, *ApJ*, 721, 715
- Du, P., Hu, C., Lu, K.-X., et al. 2014, *ApJ*, 782, 45
- Du, P., Hu, C., Lu, K.-X., et al. 2015, *ApJ*, 806, 22
- Fan, X., Burstein, D., Chen, J.-S., et al. 1996, *AJ*, 112, 628
- Haas, M., Chini, R., Ramolla, M., et al. 2011, *A&A*, 535, A73
- Ho, L. C., & Kim, M. 2015, *ApJ*, 809, 123
- Hu, C., Du, P., Lu, K.-X., et al. 2015, *ApJ*, 804, 138
- Jiang, L., McGreer, I. D., Fan, X., et al. 2015, *AJ*, 149, 188
- Kaspi, S., Smith, P. S., Netzer, H., et al. 2000, *ApJ*, 533, 631
- Kaspi, S., Maoz, D., Netzer, H., et al. 2005, *ApJ*, 629, 61
- Kaspi, S., Brandt, W. N., Maoz, D., et al. 2007, *ApJ*, 659, 997
- Kelly, B. C., Bechtold, J., & Siemiginowska, A. 2009, *ApJ*, 698, 895
- Kollatschny, W. 2003, *A&A*, 407, 461
- Kormendy, J., & Ho, L. C. 2013, *ARA&A*, 51, 511
- Magnier, E. A., Schlafly, E., Finkbeiner, D., et al. 2013, *ApJS*, 205, 20
- Matsuoka, Y., Strauss, M. A., Price, T. N., III, & DiDonato, M. S. 2014, *ApJ*, 780, 162
- Metzroth, K. G., Onken, C. A., & Peterson, B. M. 2006, *ApJ*, 647, 901
- Peterson, B. M. 1993, *PASP*, 105, 247
- Peterson, B. M., Berlind, P., Bertram, R., et al. 2002, *ApJ*, 581, 197
- Peterson, B. M., Ferrarese, L., Gilbert, K. M., et al. 2004, *ApJ*, 613, 682
- Peterson, B. M., Grier, C. J., Horne, K., et al. 2014, *ApJ*, 795, 149
- Peterson, B. M. 2014, *Space Sci. Rev.*, 183, 253
- Pozo Nuñez, F., Haas, M., Ramolla, M., et al. 2014, *A&A*, 568, A36
- Pozo Nuñez, F., Ramolla, M., Westhues, C., et al. 2015, *A&A*, 576, A73
- Rafter, S. E., Kaspi, S., Behar, E., Kollatschny, W., & Zetzl, M. 2011, *ApJ*, 741, 66
- Rafter, S. E., Kaspi, S., Chelouche, D., et al. 2013, *ApJ*, 773, 24
- Ramolla, M., Drass, H., Lemke, R., et al. 2013, *Astronomische Nachrichten*, 334, 1115
- Schlafly, E. F., Finkbeiner, D. P., Jurić, M., et al. 2012, *ApJ*, 756, 158
- Schneider, D. P., Richards, G. T., Hall, P. B., et al. 2010, *AJ*, 139, 2360
- Shen, Y., Richards, G. T., Strauss, M. A., et al. 2011, *ApJS*, 194, 45
- Shen, Y. 2013, *Bulletin of the Astronomical Society of India*, 41, 61
- Shen, Y., Brandt, W. N., Dawson, K. S., et al. 2015, *ApJS*, 216, 4
- Shen, Y., Horne, K., Grier, C. J., et al. 2015, *arXiv:1510.02802*
- Shen, Y., Greene, J. E., Ho, L. C., et al. 2015, *ApJ*, 805, 96
- Tonry, J. L., Stubbs, C. W., Lykke, K. R., et al. 2012, *ApJ*, 750, 99
- Trevese, D., Paris, D., Stirpe, G. M., Vagnetti, F., & Zitelli, V. 2007, *A&A*, 470, 491
- Wang, J.-M., Du, P., Hu, C., et al. 2014, *ApJ*, 793, 108
- Yan, H., Burstein, D., Fan, X., et al. 2000, *PASP*, 112, 691
- Zhou, X., Jiang, Z.-J., Xue, S.-J., et al. 2001, *Chin. J. Astron. Astrophys.*, 1, 372
- Zou, H., Jiang, Z., Zhou, Xu., et al. 2015, *AJ*, 150, 104
- Zu, Y., Kochanek, C. S., & Peterson, B. M. 2011, *ApJ*, 735, 80
- Zu, Y., Kochanek, C. S., Kozłowski, S., & Peterson, B. M. 2013, *arXiv:1310.6774*